



ELSEVIER

Nuclear Physics A 669 (2000) 241–265

NUCLEAR
PHYSICS **A**

www.elsevier.nl/locate/npe

Electromagnetic properties of low-excitation states in ^{191}Ir and ^{193}Ir and supersymmetry schemes

E. Bezakova ^a, A.E. Stuchbery ^a, H.H. Bolotin ^b, W.A. Seale ^{a,1}, S. Kuyucak ^c,
P. Van Isacker ^d

^a Department of Nuclear Physics, Research School of Physical Sciences and Engineering, The Australian National University, Canberra, ACT 0200, Australia

^b School of Physics, University of Melbourne, Parkville, Victoria, 3052, Australia

^c Department of Theoretical Physics, Research School of Physical Sciences and Engineering, The Australian National University, Canberra, ACT 0200, Australia

^d GANIL, B.P. 5027, F-14076 Caen, Cedex 5, France

Received 11 August 1999; received in revised form 8 October 1999; accepted 29 October 1999

Abstract

The electromagnetic properties of low-excitation states in ^{191}Ir and ^{193}Ir have been studied following Coulomb excitation. Gyromagnetic ratios were measured by the transient-field technique and level lifetimes were measured by the Doppler-shift recoil distance method. Multipolarity mixing ratios were determined from measured particle- γ angular correlations. The present lifetime and g -factor results extend the data available for comparison with theory and help discriminate between disparate experimental values reported previously in the literature. We compare the experimental data with particle-triaxial-rotor model calculations and with the predictions of the $U(6/4)$ and $U(6/20)$ supersymmetry models based on the interacting-boson-fermion model. © 2000 Elsevier Science B.V. All rights reserved.

PACS: 27.80+w; 21.10.Ky; 21.10.Tg; 23.20.Gq; 23.20.En; 21.60.Fw

Keywords: NUCLEAR REACTIONS $^{191,193}\text{Ir}(^{58}\text{Ni}, ^{58}\text{Ni}^*)$, $E = 155, 180$ MeV; $^{191,193}\text{Ir}(^{65}\text{Cu}, ^{65}\text{Cu}^*)$, $E = 130$ MeV; $^{191,193}\text{Ir}(^{32}\text{S}, ^{32}\text{S}^*)$, $E = 100$ MeV; $^{191,193}\text{Ir}(^{16}\text{O}, ^{16}\text{O}^*)$, $E = 40$ MeV; measured $\gamma(\theta, H, T)$ in polarized Gd, Fe, $\gamma(\theta, t)$ recoil, (particle) γ -coin; Coulomb excitation; $^{191,193}\text{Ir}$ levels, deduced g -factors, δ , τ ; Thin-foil transient-field IMPAC technique; Doppler-shift Recoil Distance Method; NUCLEAR STRUCTURE $^{191,193}\text{Ir}$, g , $B(E2)$, $B(M1)$, Particle-triaxial-rotor model, $U(6/4)$, $U(6/20)$ supersymmetry models

¹ Permanent address: Departamento de Física Nuclear, Instituto de Física, Universidade de São Paulo, São Paulo, Brazil.

1. Introduction

The nuclei ^{191}Ir and ^{193}Ir lie in a shape-transitional region with one more proton than the prolate osmium isotopes $^{190,192}\text{Os}$ and one proton less than the oblate platinum isotopes $^{192,194}\text{Pt}$. As such, there has been much interest in their structure from various theoretical perspectives based on geometric [1] and algebraic approaches [2]. A satisfactory description of the available experimental data before 1980 was given by Vieu et al. [3] using the particle-asymmetric-rotor model, where several Nilsson orbitals were coupled to a rigid triaxial rotor. Around the same time, supersymmetry (SUSY) schemes based on the interacting boson and interacting boson–fermion models (IBM and IBFM) were introduced [4–7], where the Pt–Ir nuclei were proposed as prime examples. In this original $U(6/4)$ SUSY model, the even Pt isotopes were described by the $O(6)$ limit of the IBM and the odd Ir isotopes by a proton hole in the $2d_{3/2}$ orbital coupled to the boson core. The desire to test the proposed nuclear SUSY resulted in many new experimental investigations of the iridium isotopes [8–17]. Discrepancies between theory and experiment found in these tests led, in turn, to the introduction of multi- j supersymmetries $U(6/m)$, $m = \sum_i (2j_i + 1)$, where all (or most) of the single-particle orbitals in the valence shell were included in the scheme [18]. In the case of iridium, the single particle orbitals involved are $\{3s_{1/2}, 2d_{3/2}, 2d_{5/2}, 2g_{7/2}\}$ and the corresponding supergroup is $U(6/20)$ [19,20]. The $U(6/20)$ SUSY model was also used in the description of odd-neutron nuclei in the $A = 130$ mass region where the even–even counterparts display a similar $O(6)$ character [21].

Despite the intense theoretical interest in these nuclei and many experimental studies, the magnetic moments of the low-lying states are not well known [15,22,23], and there are disparate values in the literature for the lifetimes of the first $5/2^+$ states in both isotopes [15,24–36]. As noted in earlier work on ^{195}Pt [37,38], the M1 properties directly

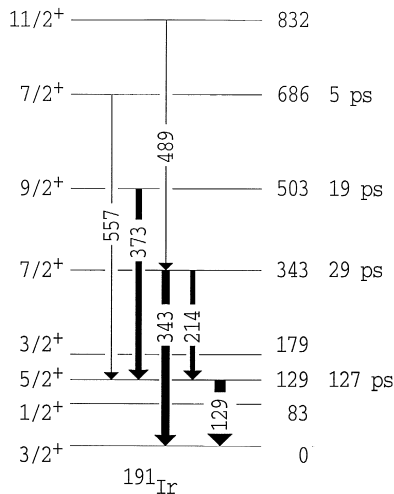
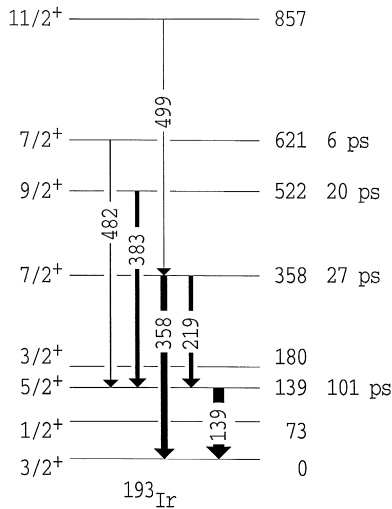


Fig. 1. Partial level scheme for ^{191}Ir showing the levels of interest. The widths of the arrows represent the intensities of the γ -ray transitions in the g -factor measurement following Coulomb excitation with 180 MeV ^{58}Ni beams (Run II). The lifetimes are the results of the present recoil-distance measurements.

Fig. 2. As for Fig. 1, but for ^{193}Ir .

probe the single-particle distributions and hence provide a more critical test of SUSY than the level energies and E2 transitions. Therefore, their accurate measurement is essential for a thorough assessment of the multi- j SUSY schemes. Besides our nuclear structure interest, the iridium isotopes ^{191}Ir and ^{193}Ir were also employed as probes in a recent study of picosecond-duration pre-equilibrium effects in hyperfine fields following ion implantation [39], for which accurate and precise lifetimes and g -factors were required.

In the present paper we report experimental studies of the electromagnetic properties of the low-lying states in ^{191}Ir and ^{193}Ir following Coulomb excitation. Some preliminary results of our transient-field g -factor measurements were reported previously [40]. Partial level schemes showing the levels of interest are presented in Figs. 1 and 2. The experimental results are analyzed using the triaxial rotor model as a benchmark and within the $U(6/4)$ and $U(6/20)$ SUSY schemes. In the $U(6/20)$ case, the effects of symmetry breaking due to the large differences in the single-particle energies are included in the calculations.

2. Experimental procedures and analysis

2.1. Angular correlation and g -factor measurements

Gyromagnetic ratios in ^{191}Ir and ^{193}Ir were measured by the transient-field (TF) technique, as in similar measurements reported previously [41–46]. States of interest were Coulomb excited using beams from the ANU 14UD Pelletron accelerator. The measurements performed and the beams employed are summarized in Table 1. Three runs (Runs I–III) were performed to determine the g -factors by the transient-field technique. In two of these measurements the transient-field precessions of the states of

Table 1
Summary of precession and angular correlation experiments

Run	Type of experiment ^a	Detector angles ^b	Target ^c	Beam	E_{Beam} [MeV]
I	TF g -factors	$0^\circ, \pm 30^\circ, \pm 45^\circ, \pm 55^\circ, \pm 65^\circ$	A (Gd)	^{58}Ni	155
II	TF g -factors	$0^\circ, \pm 30^\circ, \pm 45^\circ, \pm 55^\circ, \pm 60^\circ, \pm 65^\circ$	B (Gd)	^{58}Ni	180
III	TF g -factors	$\pm 30^\circ$	A (Gd)	^{65}Cu	130
IV	TF precessions	$\pm 30^\circ, \pm 45^\circ, \pm 55^\circ, \pm 65^\circ$	C (Fe)	^{32}S	100
V	SF precessions	$0, \pm 30^\circ, \pm 35^\circ, \pm 45^\circ, \pm 55^\circ, \pm 65^\circ$	D (Fe)	^{16}O	40

^a TF g -factors: transient-field measurement of relative g -factors; TF precessions: study of the transient-field strength for Ir in Fe; SF precessions: study of the static-field strength for Ir in Fe.

^b Angles at which the pair of detectors in the forward quadrants were placed. The backward-placed detectors were at $\pm 115^\circ$ in all cases.

^c Target details are in Table 2. The ferromagnetic hosts are indicated in parentheses.

interest in ^{191}Ir and ^{193}Ir were measured simultaneously with those of the first 2^+ state in ^{198}Pt as their ions traversed a polarized Gd foil. ^{198}Pt was chosen to calibrate the transient field because its g -factor is well known [47] and ^{198}Pt does not produce γ -ray lines that would obscure lines of interest in the iridium isotopes. The measurements with Fe hosts were performed primarily to study the static and transient hyperfine magnetic fields for Ir in Fe [39,48]; they are reported here briefly in relation to the present g -factor measurements.

Details of the targets are presented in Table 2. The ferromagnetic foils were rolled to the required thickness and annealed under vacuum. The Ir and Pt layers were then sputtered onto the upstream side. Finally, the Cu or Pb backing layers were evaporated on the downstream side of the Fe or Gd foils. For additional mechanical support and improved thermal contact with the cold-finger, the targets were pressed onto a thicker ($\sim 12 \mu\text{m}$) Cu foil using an evaporated layer of indium as adhesive. Throughout the measurements with Gd host foils, the target temperature was maintained at ≈ 90 K. The measurements with Fe hosts were performed at room temperature. The ferromagnetic foils were polarized perpendicular to the γ -ray detection plane by a small electromagnet and the direction of this polarizing field was reversed automatically, approximately every 15 minutes.

The magnetizations of the targets at temperatures and applied field intensities close to those that pertained during the precession measurements were measured using the

Table 2
Target details

Target	L_{tgt} [$\text{mg} \cdot \text{cm}^{-2}$] ^a			Host ^b	L_{host} ^b [$\text{mg} \cdot \text{cm}^{-2}$]	M ^b [T]	Backing ^c	L_{back} ^c [$\text{mg} \cdot \text{cm}^{-2}$]
	^{191}Ir	^{198}Pt	^{193}Ir					
A		0.26	1.08	Gd	5.45	0.186(6)	Cu	6.4
B			1.28	Gd	5.94	0.181(5)	Cu	7.2
C	0.34	0.15	0.40	Fe	1.61	0.175(9)	Pb	≥ 4
D	0.39	0.15	0.51	Fe	1.63	0.180(9)	Cu	4.5

^a Thickness of target layers, L_{tgt} , in the order encountered by the beam (left to right in table).

^b Ferromagnetic host, its thickness, L_{host} , and magnetization, M .

^c Nonmagnetic backing layer and its thickness, L_{back} .

Rutgers magnetometer [49]. The main source of uncertainty in these measured magnetizations comes from uncertainties in the dimensions of the foils, estimated to be $\sim 3\%$ for the Gd foils and $\sim 5\%$ for the Fe foils. In all cases the magnetization achieved is consistent with the maximum routinely achieved for the polarizing fields and temperatures that pertained.

The thicknesses of the target layers were chosen to ensure that, in all runs, the Pt and Ir ions left the Gadolinium layer and stopped in the non-magnetic backing layer. Details of the reaction kinematics are given in Table 3. In preparing this table, we have employed the stopping powers of Ziegler et al. [50], although there is evidence that they tend to overestimate the stopping of $A \sim 200$ ions in Gd [40].

Backscattered beam ions were recorded in an annular silicon surface barrier (SSB) counter which subtended the angular range between 150° and 167° to the beam axis. The precessions of the nuclei were measured by placing two Ge γ -ray detectors in the forward direction, usually at $\pm 30^\circ$ but also often at $\pm 65^\circ$ to the beam direction, where the particle- γ angular correlations for most of the transitions of interest have near maximal slope and hence give near-optimum sensitivity to the nuclear precessions. A pair of detectors remained at $\pm 115^\circ$ to the beam direction throughout the measurements. Precession data were also taken during the angular correlation measurements.

Unperturbed particle- γ -ray angular correlations were measured during each run. The two detectors in the backward quadrants remained at $\pm 115^\circ$ to serve as monitors, while the forward detectors were placed at a sequence of angles between 0° and $\pm 65^\circ$ to the beam direction, as listed in Table 1. For the transient-field measurements and those static-field measurements where the precession angle is small (≤ 100 mrad), the unperturbed angular correlation is obtained by adding together the perturbed angular correlations for field ‘up’ and field ‘down’.

The angular correlations were analyzed as described in previous work [45,46]. Initially, we fit the pure E2 transitions with no free parameters but an overall normaliza-

Table 3
Kinematics and transient-field precessions

Run	Nucleus	E_i^a [MeV]	E_e^a [MeV]	$\langle v/v_0 \rangle^b$	T_{tgt}^c [ps]	T_{host}^c [ps]	$-\phi_{\text{CR}}^d$ [mrad]	$-\phi_{\text{RU}}^d$ [mrad]	$-\phi_{\text{exp}}^e$ [mrad]
I	$^{191,193}\text{Ir}$	92	13	2.78	0.03	1.1	220	170	171(7)
I	^{198}Pt	85	10	2.55	0.06	1.3	230	180	178(7)
II	$^{191,193}\text{Ir}$	108	15	2.98	0.03	1.2	233	178	182(7)
III	$^{191,193}\text{Ir}$	80	8	2.47	0.03	1.3	229	181	179(9)
III	^{198}Pt	75	6	2.26	0.06	1.4	237	191	187(9)
IV	$^{191,193}\text{Ir}$	42	12	2.20	0.03	0.43			42.4 ^f
IV	^{198}Pt	41	11	2.13	0.03	0.45			42.9 ^f

^a $E_i(E_e)$ calculated average energy of recoils on entry into (exit from) the ferromagnetic host layer of the target. (The calculated exit energies underestimate the actual exit energies. See text.)

^b Average velocity of recoils traversing the Fe foil ($v_0 = c/137$).

^c T_{tgt} [T_{host}] average time spent by recoils in the Ir and ^{198}Pt [Gd or Fe] target layers.

^d Estimated transient-field precession based on the Chalk River (CR) [54,55] and Rutgers (RU) [56] parametrizations of the TF for Gd hosts. $\phi = \Delta\theta/g$.

^e Measured transient-field precessions for ^{198}Pt and the values for $^{191,193}\text{Ir}$ scaled from them.

^f The CR and RU parametrizations are not applicable for Pt and Ir in Fe. These estimated transient-field precessions are based on the linear fit to data reported in Ref. [58].

tion factor and a possible small offset of the detection angles from their nominal values. Then, once this offset has been determined, we fit the mixed transitions with only the normalization and the mixing ratio allowed to vary.

Analysis of the g -factor measurements was performed as described previously [41–46]. While the feeding intensity is not prohibitive in any of the runs, the three runs with different beams were employed to vary the relative Coulomb excitation probabilities for the low-lying states, particularly to provide cross checks on the corrections for feeding applied to the $5/2_1^+$ states.

2.2. Relative Coulomb-excitation cross sections

Relative Coulomb-excitation cross sections were determined for the levels in ^{191}Ir and ^{193}Ir during the angular correlation measurements. As well as being required to make the feeding corrections in the g -factor measurements, these can be used to estimate the relative E2 matrix elements in ^{191}Ir and ^{193}Ir (cf. [16,17]), and hence help discriminate between disparate lifetime results in the literature [15,24–36] (see below).

2.3. Recoil-distance lifetime measurements

The lifetimes of the lowest few states in ^{191}Ir and ^{193}Ir were measured by the recoil-distance method (RDM). A layer of natural iridium $\sim 500 \mu\text{g}/\text{cm}^2$ thick was sputtered onto the downstream side of a stretched nickel foil $830 \mu\text{g}/\text{cm}^2$ thick. Beams of ^{32}S with an energy of 100 MeV impinged upon the Ni side of the target foil and encountered the Ir layer with an energy of ~ 91 MeV. The measured recoil velocity determined from several lines at several distances was $v/c = 2.11(1)\%$. Recoils were stopped in a stretched $\sim 10 \text{ mg}/\text{cm}^2$ thick Ta foil. The target–stopper distance was varied from 23 to 2400 μm , corresponding to flight times between about 4 ps and 400 ps.

The de-excitation γ -rays from ^{191}Ir and ^{193}Ir were recorded by two Ge detectors, placed at 0° and 30° to the beam, in coincidence with backscattered beam ions. The backscattered ions were detected in an annular SSB counter which subtended the angular range 156° – 168° to the beam axis. The total number of backscattered particles in singles was recorded to provide a normalization for each target–stopper distance. This allows for an analysis of unshifted, u , and shifted, s , peak areas individually, along with the usual ratio $R = u/(u + s)$.

For the analysis we employed a computer code based on the formalism of Sturm and Guidry [51], but with an improved treatment of the combination of feeding and vacuum-deorientation corrections [52]. The required unperturbed angular correlations were taken from our work described above and appropriately modified for the different particle detector and γ -ray detector locations. The relative excitation probabilities required to make feeding corrections were determined from the observed γ -ray intensities and confirmed by rescaling the observed yields in the g -factor and angular correlation measurements according to the calculated Coulomb-excitation cross sections.

As the extracted lifetimes were found to be insensitive to the vacuum deorientation parameters, we set $\tau_2 = 15$ ps, with $\tau_4 = 0.3\tau_2$, and assumed no hard-core effect at longer times, consistent with the analysis of earlier measurements on the even platinum

isotopes [53]. The computer program fits the ratio data and then predicts the u and s peak intensities within a single normalization factor.

We found that the intensity of the peaks in the unshifted spectra did not always go to zero at longer flight times. This is often found in RDM measurements and is possibly due to small contaminant peaks from nuclear reactions and/or to a small build up of some target material on the stopper. It can be accounted for either by excluding the longer-distance data from the fits, or by including a constant ‘background’ when fitting the unshifted peak intensity. (We confirmed that these two procedures gave consistent lifetime results.)

3. Experimental results

3.1. Angular correlations, mixing ratios and g -factors

Examples of γ -ray spectra recorded in coincidence with backscattered beam ions during Runs I–III are shown in Fig. 3. Particle- γ angular correlations measured during Run I are presented in Fig. 4. The present measured mixing ratios are compared with previous results in Table 4. Generally, our mixing ratios are more precise than the previous values, with which they agree.

Table 5 summarizes the results of the transient-field precession measurements from Runs I–III. The observed precessions, the precessions of the levels after correction for the effects of feeding and finite level lifetimes and the relative excitation cross sections

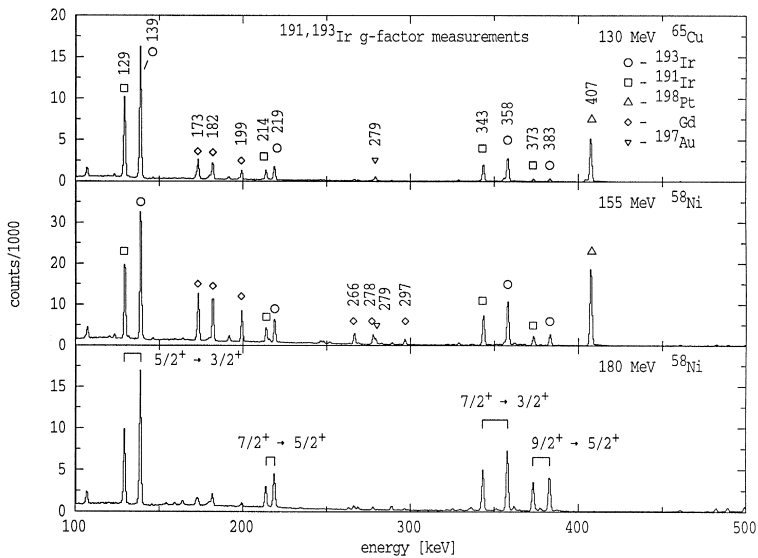


Fig. 3. Examples of γ -ray spectra recorded in coincidence with backscattered beam ions, following Coulomb excitation, in the transient-field g -factor measurements. Upper: 130 MeV ^{65}Cu (Run III). Middle: 155 MeV ^{58}Ni (Run I). Lower: 180 MeV ^{58}Ni (Run II). (The 279 keV line comes from a small amount of ^{197}Au which was sputtered from the sample substrate during the deposition of the ^{198}Pt layer.)

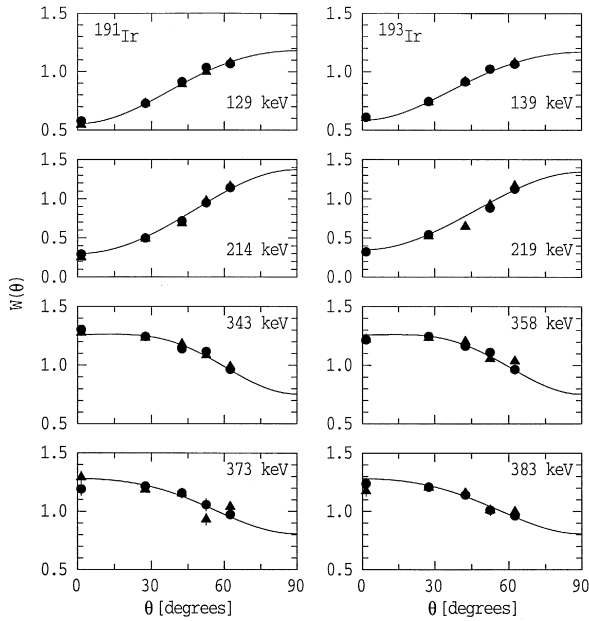


Fig. 4. Particle- γ angular correlations for transitions in ^{191}Ir and ^{193}Ir , measured during Run I (155 MeV ^{58}Ni beam). The experimental data are compared with the calculated angular correlations. For the mixed multipolarity transitions, the mixing ratio is a free parameter.

are shown. To obtain the absolute values of the g -factors, we define the integral transient-field strength for each atomic species and each run as $\phi = \Delta\theta/g$, where $\Delta\theta$ is the precession of the nucleus (corrected for finite lifetime effects and feeding from higher populated states) and g is the g -factor of the nuclear level. In Runs I and III, these transient-field strengths for Ir in Gd were calibrated relative to the simultaneously measured TF strengths for ^{198}Pt in Gd, after taking into account a small correction for the different atomic numbers and stopping powers of the two species. The measured transient-field strengths for Pt in Gd are presented along with the predictions of the Chalk River [54,55] and Rutgers [56] parametrizations in Table 3; the integral field-strengths adopted for the iridium isotopes are also shown. In agreement with the work of

Table 4
Comparison of mixing ratios in ^{191}Ir and ^{193}Ir

Isotope	E_x (keV)	E_γ (keV)	Transition	δ	
				present work	NDS ^a
^{191}Ir	129	129	$5/2^+ \rightarrow 3/2^+$	-0.402 ± 0.007	-0.40 ± 0.01
	343	214	$7/2^+ \rightarrow 5/2^+$	-0.342 ± 0.007	-0.34 ± 0.04
	686	557	$7/2^+ \rightarrow 5/2^+$	-0.98 ± 0.12	-1.34 ± 0.16
^{193}Ir	139	139	$5/2^+ \rightarrow 3/2^+$	-0.362 ± 0.006	-0.329 ± 0.012
	358	219	$7/2^+ \rightarrow 5/2^+$	-0.280 ± 0.009	-0.34 ± 0.04
	621	482	$7/2^+ \rightarrow 5/2^+$	-0.89 ± 0.13	-1.02 ± 0.19

^a Nuclear Data Sheets [22,23].

Table 5
Measured transient-field precessions in ^{191}Ir and ^{193}Ir

Run	J^π	^{191}Ir				^{193}Ir			
		E_x	$P(J)/P(\frac{5}{2})^a$	$\Delta\theta_{\text{obs}}^b$	$\Delta\theta^c$	E_x	$P(J)/P(\frac{5}{2})^a$	$\Delta\theta_{\text{obs}}^b$	$\Delta\theta^c$
		[keV]	[%]	[mrad]	[mrad]	[keV]	[%]	[mrad]	[mrad]
I	$5/2^+$	129	100(4)	-62(3)	-58(5)	139	100(4)	-64.9(2.4)	-60(3)
	$7/2^+$	343	36.8(5)	-67(3)	-68(3)	358	36.9(5)	-73.3(2.6)	-75(3)
	$9/2^+$	503	6.5(3)	-90(13)	-93(14)	552	4.8(1)	-114(12)	-117(13)
II	$5/2^+$	129	100(2)	-70(4)	-63(7)	139	100(2)	-74.9(2.6)	-73(5)
	$7/2^+$	343	56.8(5)	-73(3)	-68(5)	358	55.7(5)	-79(3)	-82(4)
	$9/2^+$	503	29.3(3)	-92(9)	-95(10)	552	17.6(2)	-75(7)	-71(9)
	$7/2^+$	686	5.1(2)	-38(15)	-42(17)	621	5.7(1)	-53(7)	-59(8)
	$11/2^+$	832	3.7(1)	-100(28)	-111(31)	857	6.3(1)	-79(21)	-89(23)
III	$5/2^+$	129	100(3)	-55(5)	-51(6)	139	100(3)	-59(4)	-57(5)
	$7/2^+$	343	18.5(3)	-87(8)	-88(8)	358	19.1(3)	-76(7)	-78(7)

^a Measured Coulomb-excitation cross section relative to the first $5/2^+$ state.

^b Observed transient-field precession, including the effects of (i) feeding from higher excited states and (ii) decays which take place while the ions are in transit through the ferromagnetic foil.

^c Precession of the individual level, after corrections for feeding and finite lifetime effects. Within each run, relative $\Delta\theta$ values give relative g -factors.

Tanczyn et al. [57], the TF strength measured for Pt in Gd agrees with the Rutgers parametrization [56], but is about 20% smaller than that predicted by the Chalk River parametrization [54,55]. For the present purposes of scaling the measured precessions for platinum to apply for iridium, however, the difference between the two parametrizations is not statistically significant. Table 6 shows the absolute g -factors obtained from Runs I–III and the average adopted values.

As noted above, Runs IV and V were performed primarily to study the hyperfine field strengths for iridium in iron. We present them here because similar measurements were used by Kölbl et al. [15] to determine the g -factors in ^{191}Ir and ^{193}Ir . The results of

Table 6
Measured g -factors in ^{191}Ir and ^{193}Ir

Isotope	E_x (keV)	J^π	g -factor ^a			
			Run I	Run II	Run III	Adopted
^{191}Ir	129	$5/2^+$	0.34 ± 0.03	0.35 ± 0.04	0.29 ± 0.04	0.322 ± 0.022
	343	$7/2^+$	0.40 ± 0.02	0.37 ± 0.03	0.49 ± 0.05	0.401 ± 0.018
	503	$9/2^+$	0.54 ± 0.08	0.52 ± 0.06	–	0.53 ± 0.05
	686	$7/2^+$	–	0.23 ± 0.09	–	0.23 ± 0.09
	832	$11/2^+$	–	0.61 ± 0.17	–	0.61 ± 0.17
^{193}Ir	139	$5/2^+$	0.35 ± 0.02	0.40 ± 0.03	0.32 ± 0.03	0.356 ± 0.016
	358	$7/2^+$	0.44 ± 0.02	0.45 ± 0.03	0.43 ± 0.05	0.441 ± 0.016
	552	$9/2^+$	0.68 ± 0.08	0.39 ± 0.05	–	0.48 ± 0.04
	621	$7/2^+$	–	0.33 ± 0.04	–	0.33 ± 0.04
	857	$11/2^+$	–	0.49 ± 0.13	–	0.49 ± 0.13

^a g -factors evaluated from the precessions $\Delta\theta$ given in Table 5 using the transient-field strengths ϕ given in the final column of Table 3, $g = \Delta\theta/\phi$.

Table 7

Transient-field measurements for $^{191,193}\text{Ir}$ and ^{198}Pt traversing an iron host (Run IV)

Nucleus	J_i^π	$P(J)/P(5/2)$ ^a	$\Delta\theta_{\text{obs}}$ ^b [%]	$\Delta\theta$ ^c [mrad]	g ^d [mrad]
^{191}Ir	$5/2_1^+$	100(4)	−15.2(23)	−13(4)	0.31(9)
	$7/2_1^+$	51(1)	−15.7(23)	−15.8(23)	0.37(6)
	$9/2_1^+$	7.9(3)	−32(15)	−32(15)	0.8(4)
^{193}Ir	$5/2_1^+$	100(4)	−15.3(17)	−12(3)	0.29(7)
	$7/2_1^+$	51(1)	−20.4(21)	−19.4(19)	0.45(5)
	$9/2_1^+$	5.8(2)	−39(13)	−39(13)	0.9(3)
^{198}Pt	2_1^+	100	−14.4(9)	−14.5(9)	0.34(2)

^a Measured relative populations of the states within each nucleus.^b Observed precession of the level J_i^π , including the effects of feeding.^c Precession of the level J_i^π , corrected for feeding.^d g -factor, $g = \Delta\theta/\phi$, where $\phi = 42.4[42.9]$ mrad for Ir[Pt]; see text.

the transient-field measurements from Run IV are summarized in Table 7. Assuming that the transient-field strength for iridium in iron has the same form as that for platinum in iron [58], we obtain g -factors that agree, within relatively large statistical errors, with those obtained in Runs I–III. However, neither the relative nor the absolute g -factors obtained agree with those of Kölbl et al. [15]. The difference in the absolute g -factors originates, in part, from the $g(5/2_1^+)$ values adopted from their static-field measurements which were interpreted with incorrect lifetimes values (see below). It is not clear why there is a discrepancy between their relative g -factors and ours, but it would be explained if, for example, some fraction of the recoiling iridium ions stopped in the iron layer in their measurements.

The results of our static-field measurements (Run V) have been presented and discussed elsewhere [39] in relation to pre-equilibrium effects in static hyperfine magnetic fields following ion implantation. Some of the results are summarized in Table 8. It is evident from these data that the effective static-field strength experienced by the implanted ions depends on the lifetime of the nuclear state. This has been interpreted in

Table 8

Measured precessions and static hyperfine field strengths for ^{191}Ir and ^{193}Ir in Fe hosts

Nucleus	Level	g ^a	τ ^b [ps]	$\Delta\theta_c$ ^c [mrad]	$\omega\tau$ ^d [mrad]	B_{IMPAC} [T]
^{191}Ir	$5/2_1^+$	0.322(20)	127.6(20)	−8(1)	207(3)	106(7)
	$7/2_1^+$	0.401(18)	29.5(11)	−10(1)	51(2)	89(6)
^{193}Ir	$5/2_1^+$	0.356(16)	100.5(15)	−9(1)	177(3)	103(5)
	$7/2_1^+$	0.441(16)	27.0(8)	−11(1)	48(2)	84(5)
^{198}Pt	2_1^+	0.314(11)	33.0(16)	−7(1)	44(2)	89(8)

^a g -factors from present transient-field measurements relative to the 2_1^+ state in ^{198}Pt [47].^b Average meanlives for ^{191}Ir and ^{193}Ir from present work and Refs. [16,17]. The meanlife in ^{198}Pt is from Ref. [59].^c Calculated transient-field precessions. See Refs. [39,48] and text.^d Present results. For ^{198}Pt the weighted average of present and previous results [60] is given.

Table 9

Comparison of measured $5/2_1^+$ -state g -factors in ^{191}Ir and ^{193}Ir

Isotope	τ [ps] ^a	g -factor	Method ^b	Reference
^{191}Ir	127 ± 2	0.322 ± 0.020	TF (Gd)	Run I–III
		0.31 ± 0.09	TF (Fe)	Run IV
		0.276 ± 0.017	IPAC ^c	[32]
		0.392 ± 0.030	IPAC ^c	[63]
		0.281 ± 0.024	IPAD,ME ^c	[64]
		0.28 ± 0.04	RIG ^c	[62]
^{193}Ir	101 ± 2	0.356 ± 0.016	TF (Gd)	Run I–III
		0.29 ± 0.07	TF (Fe)	Run IV
		0.24 ± 0.05	IPAC ^c	[61]
		0.21 ± 0.05	IPAC ^c	[63]
		0.33 ± 0.05	RIG ^c	[62]

^a Adopted meanlife from present RDM measurements.^b TF: transient field technique with the designated host; IPAC: Integral perturbed angular correlations in radioactivity measurement; IPAD,ME: Integral perturbed angular distributions of resonance-scattered γ -rays; RIG: Recoil into gas.^c Lifetime-dependent technique.

terms of the lifetime of the thermal spike that accompanies ion implantation, causing the static field to be absent for about 7 ps after implantation for typical implantation perturbed angular correlation (IMPAC) measurements [39]. As such, the static-field

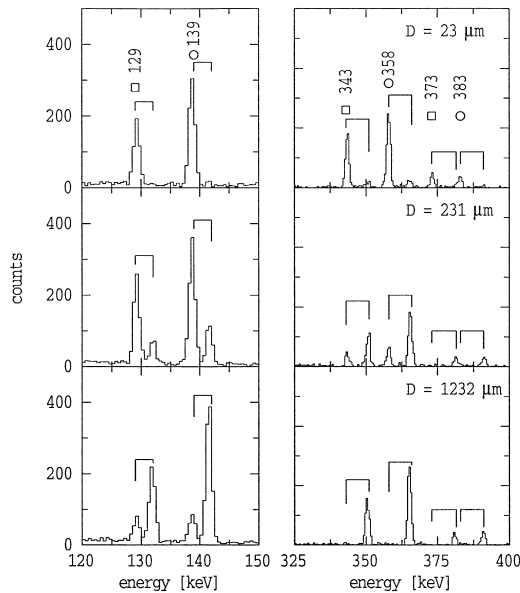


Fig. 5. Examples of γ -ray spectra recorded in the detector at 0° to the beam during the recoil-distance lifetime measurements. The target–stopper separations are (top to bottom) $23 \mu\text{m}$, $231 \mu\text{m}$ and $1232 \mu\text{m}$, corresponding to the flight times 4 ps, 39 ps and 205 ps, respectively. The positions of the shifted and unshifted peaks are indicated.

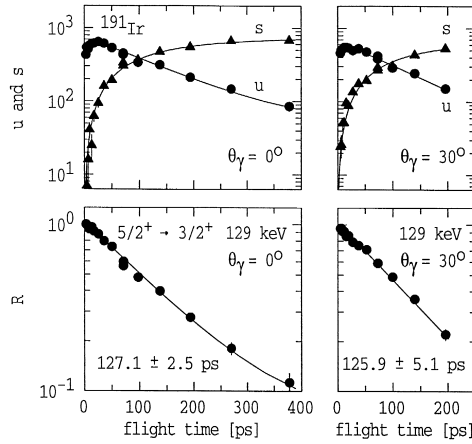


Fig. 6. Shifted (s), unshifted (u) and ratio (R) data and fits for the 129 keV $5/2_1^+ \rightarrow 3/2_1^+$ transition in ^{191}Ir . Once the lifetime is varied to fit the ratio data (lower panels), the fits to shifted and unshifted data are determined within a single normalization parameter.

IMPAC technique cannot be employed to determine the g -factors of states with lifetimes of about 30 ps with an accuracy better than $\sim 20\%$. Rather than attempting to correct for this effect, we exclude the present and previous IMPAC measurements from the comparisons of measured g -factors presented below.

The static-field precessions we observe for the first $5/2^+$ states in ^{191}Ir and ^{193}Ir agree with those reported by Kölbl et al. [15], but those for the first $7/2^+$ states do not agree, despite relatively large uncertainties in the previous measurements. The reason for this disparity is not known; however as our measurements are more precise, and as the simultaneously measured precession of the 2_1^+ state in ^{198}Pt (which has a similar magnitude) agrees with earlier work [60], there are strong reasons to believe that our results are correct.

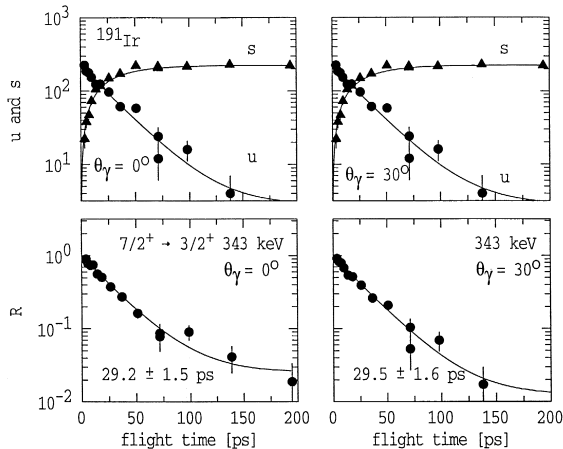


Fig. 7. As for Fig. 6, but for the 343 keV $7/2_1^+ \rightarrow 5/2_1^+$ transition in ^{191}Ir .

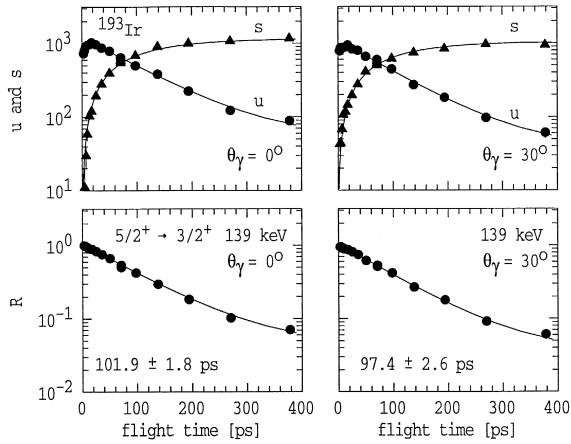


Fig. 8. As for Fig. 6, but for the 139 keV $5/2_1^+ \rightarrow 3/2_1^+$ transition in ^{193}Ir .

Our results for the first $7/2^+$ and higher states are either the first measurements reported or are much more precise than those obtained previously. On the other hand, there have been several measurements of the g -factors of the $5/2_1^+$ states by a variety of techniques [15,32,61–64]. These (excluding the static-field IMPAC measurements for the reason noted above) are compared in Table 9. Where applicable, the results have been corrected to correspond to the present adopted lifetimes (see below) and, for consistency, the room-temperature static field in the radioactivity measurements is taken to be $B_{\text{st}}(\text{IrFe}) = -135.8 \pm 1.7 \text{ T}$ [65].

For the first $5/2^+$ states, the g -factors obtained from our transient-field measurements are generally larger than the previous results, but for ^{191}Ir , where the statistical uncertainties are much smaller than for ^{193}Ir , the difference is hardly significant. The previous IPAC measurements for ^{193}Ir are not in very good agreement with the present

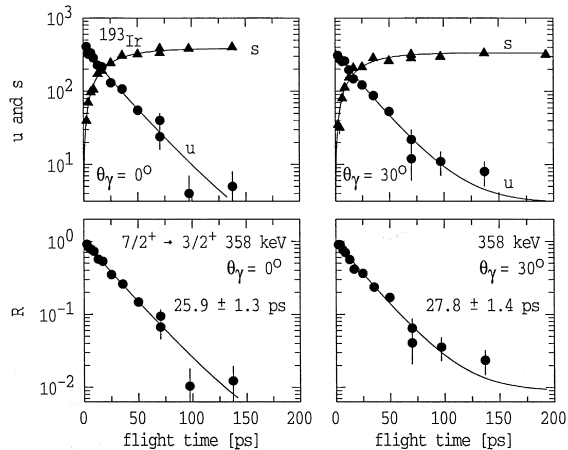


Fig. 9. As for Fig. 6, but for the 358 keV $7/2_1^+ \rightarrow 5/2_1^+$ transition in ^{193}Ir .

TF measurements, despite their relatively large uncertainties. As these older IPAC measurements for both ^{191}Ir and ^{193}Ir were made with NaI detectors, it would be appropriate to repeat the measurements with high-resolution Ge detectors. The present TF measurements agree quite well with the recoil-in-gas measurements [62], but again the uncertainties are relatively large.

3.2. Lifetimes

Some examples of the γ -ray spectra from our RDM lifetime measurements are shown in Fig. 5. In view of the disparate lifetime values in the literature for the $5/2_1^+$ states in both ^{191}Ir and ^{193}Ir , we show in Figs. 6, 7, 8, 9 our complete set of shifted-, unshifted- and ratio data, and the corresponding fits, for the lowest $5/2^+$ and $7/2^+$ states. The internal consistency of our data is evident: note that once the ratio data are fitted in each

Table 10
Comparison of meanlives in ^{191}Ir and ^{193}Ir

Isotope	E_x (keV)	J^π	Meanlife [ps]				
			RDM previous ^a	Radioactive decay	Mössbauer	Coulomb excitation	RDM present
^{191}Ir	129	$5/2^+$	174 ± 7	189 ± 14 ^b 182 ± 16 ^c 115 ± 23 ^h	128 ± 3 ^c 144 ± 10 ^f 132 ± 2 ⁱ	131 ± 4 ^d 141 ± 14 ^g 132 ± 11 ^j	126.8 ± 2.3
	343	$7/2^+$	30.8 ± 4.4	–	–	29.6 ± 1.3 ^d 30.6 ± 3.6 ^g 33 ± 6 ^j	29.4 ± 2.2
^{193}Ir	503	$9/2^+$	18.9 ± 4.6	–	–	–	19.3 ± 2.7
	139	$5/2^+$	133 ± 6	127 ± 13 ^k 111 ± 25 ^m 108 ± 15 ⁿ 96 ± 12 ^o	115 ± 3 ^c	100.5 ± 3.8 ^l 115 ± 15 ^g 108 ± 11 ^j 103 ± 10 ^p	100.5 ± 1.5
	358	$7/2^+$	29.4 ± 3.5	–	–	27.3 ± 1.2 ^l 29.3 ± 3.2 ^g 28.4 ± 4.2 ^j	26.8 ± 1.0
	522	$9/2^+$	16.5 ± 5.8	–	–	–	20.1 ± 3.2
	621	$7/2^+$	8.8 ± 2.4	–	–	–	6.3 ± 0.7

^a Ref. [15].
^b Ref. [25].
^c Ref. [33].
^d Ref. [16].
^e Ref. [31].
^f Ref. [32].
^g Ref. [28].
^h Ref. [26].
ⁱ Ref. [36].
^j Ref. [35].
^k Ref. [27].
^l Ref. [17].
^m Ref. [29].
ⁿ Ref. [34].
^o Ref. [30].
^p Ref. [24].

case, the associated u and s values are predicted within a single normalization factor. The rise in the unshifted peak intensity observed for the 129 and 139 keV transitions at short flight times is due to the combined effects of feeding from the higher states and vacuum deorientation [52].

The present lifetime results are summarized and compared with previous measurements in Table 10. It is apparent that the present and previous measurements are in agreement for the $7/2_1^+$ and higher states, but that there is a range of values reported for the lifetimes of the first $5/2_1^+$ states in both isotopes. Our results for the $5/2_1^+$ states do not agree with the only previous RDM measurement [15], but they agree well with the Coulomb excitation measurements [16,17,24,28,35] and with the Mössbauer measurements in ^{191}Ir [36].

Some authors, including the compilers of Nuclear Data Sheets [22], have dismissed the Mössbauer measurements on the grounds that possible spurious effects may broaden the absorption line, consequently reducing the level lifetime. A subsequent Mössbauer study by Wagoner, Mullen and Schupp [36] however, has concluded that, if present, the purported broadening would have been clearly evident in their data analysis; but instead they find that there is no evidence for such broadening. Our lifetime measurements support these conclusions. Furthermore, the present observed relative cross sections are consistent with the $B(E2)$ values implied by our measured lifetimes (and with the $B(E2)$ values from previous Coulomb excitation studies), but are not consistent with the $B(E2)$ values implied by the longer lifetimes reported for the $5/2_1^+$ states of $^{191,193}\text{Ir}$ in Refs. [15,22,23]. For example, if we normalize to the previously measured $B(E2)$ values for

Table 11
M1 and E2 transition rates in ^{191}Ir and ^{193}Ir

Isotope	E_x [keV]	J_i^π	τ_m^a [ps]	J_f^π	E_γ [keV]	I_γ^b	α_T^c	δ^c	$B(M1)$ [μ_N^2]	$B(E2)$ [e^2b^2]
^{191}Ir :	129.4	$5/2^+$	127(2)	$1/2^+$	47.1	0.0093(7)	147	∞	–	0.067(7)
				$3/2^+$	129.4	100(6)	2.84	–0.402(7)	0.046(1)	0.64(2)
	343.4	$7/2^+$	29(2)	$5/2^+$	213.9	59(2)	0.689	–0.342(7)	0.051(3)	0.186(16)
				$3/2^+$	343.5	100(2)	0.065	∞	–	0.28(2)
502.8	$9/2^+$	19(3)	$7/2^+$	159.5	9.1(5)	1.23	[1] ^d	–	–	
			$5/2^+$	373.4	100(2)	0.051	∞	–	0.46(7)	
^{193}Ir	138.9	$5/2^+$	101(2)	$3/2^+$	138.9	100	2.35	–0.362(6)	0.056(1)	0.54(2)
				$5/2^+$	218.8	62(3)	0.646	–0.280(9)	0.056(3)	0.13(1)
	357.7	$7/2^+$	27(1)	$3/2^+$	357.7	100(2)	0.058	∞	–	0.25(1)
				$7/2^+$	164.2	9.9(7)	1.13	[1] ^d	–	–
	521.9	$9/2^+$	20(3)	$5/2^+$	383.0	100(2)	0.048	∞	–	0.39(6)
				$5/2^+$	259.8	5(2)	0.436	[1] ^d	–	–
	621.2	$7/2^+$	6.3(7)	$7/2^+$	264.0	10(2)	0.395	–0.26(11)	0.023(5)	0.032(26)
				$5/2^+$	482.2	100(2)	0.053	–0.93(11)	0.021(3)	0.11(2)
$3/2^+$				621.2	74(4)	0.0144	∞	–	0.052(6)	

^a Meanlives from present RDM measurements.

^b γ -ray intensities from the present work and Nuclear Data Sheets [22,23].

^c Total conversion coefficients, mainly from Nuclear Data Sheets [22,23]. Mixing ratios from present work and Nuclear Data Sheets.

^d To evaluate the transition rates for the other decays from this state, the mixed multipolarity transition with unknown mixing ratio was assigned $\delta = 1 \pm 1$.

the $7/2_1^+$ states (for which the lifetime and $B(E2)$ values are not controversial), our observed cross sections imply meanlives of about 139 ± 6 ps and 98 ± 4 ps for the $5/2_1^+$ states in ^{191}Ir and ^{193}Ir , respectively.

It now appears, therefore, that it is the previous RDM measurement of the $5/2_1^+$ state lifetimes and some of the early decay measurements (which are difficult for such short-lived states) that are in error. Concerning the previous RDM measurement, it may be relevant that the fits to the γ -ray yields for stopped nuclei shown in Fig. 4 of Ref. [15] approach zero at time zero, which is unphysical. It is unfortunate that Kölbl et al. [15] do not mention feeding corrections in their analysis of the RDM data for the $5/2_1^+$ states, for these corrections have more influence on the extracted lifetimes than the vacuum deorientation parameters.

The M1 and E2 transition rates determined from the present level lifetimes and mixing ratios are presented in Table 11. Note that our measured γ -ray branching ratios for the 358 keV state in ^{193}Ir agree with those of Mundy et al. [14] but disagree with a recent measurement by Drissi [66]. The 219 keV transition may have been contaminated by a transition from the $7/2^-$ state at 299 keV in Ref. [66], but the population of such negative-parity states is strongly suppressed in Coulomb excitation.

4. Theoretical calculations

4.1. Particle-triaxial-rotor model

Asymmetric rotor model calculations have been performed previously for ^{191}Ir and ^{193}Ir by several authors, e.g. Refs. [3,16,17,66]. Generally the E2 properties of these nuclei are well described by particle-triaxial-rotor calculations based on the Nilsson potential, in which the deformations are about $\epsilon \sim 0.17$ and $\gamma \sim 25^\circ$.

We have performed calculations similar to those reported previously to (i) provide more detailed comparisons with the M1 properties and g -factors and (ii) provide a benchmark for comparison with our broken $U(6/20)$ supersymmetry model calculations. In contrast with some of the earlier work, we have employed a standard set of model parameters and have not fine-tuned them to improve the agreement between theory and experiment.

Calculations were made with the modified oscillator version of the particle-plus-triaxial-rotor code of Semmes, Ragnarsson and co-workers [67]. The deformation was set to $\epsilon_2 = 0.17$ for ^{191}Ir and $\epsilon_2 = 0.16$ for ^{193}Ir , with $\epsilon_4 = 0$ and $\gamma = 25^\circ$ in both cases. As in the calculations of McGowan et al. [16,17], we included the orbits numbered 19,20 and 21, which correspond mainly to the Nilsson orbits $5/2^+[402]$, $1/2^+[411]$ and $3/2^+[402]$. (See also the discussion of Vieu et al. [3].) However, unlike McGowan et al., we used the ‘standard’ parameters for the Nilsson potential given by Bengtsson and Ragnarsson [68]. The energy of the first-excited state of the core was set to $E(2^+) = 210(220)$ keV for ^{191}Ir (^{193}Ir). The pairing parameters were the same as employed by McGowan et al. [16,17]. The Coriolis interactions were not attenuated. In the calculations of the g -factors and $B(M1)$ strengths, the collective g -factor was set to $Z/A = 0.40$ and the spin g -factor was quenched to 0.75 times that of the free nucleon.

Table 12

Comparisons of quadrupole moments and g -factors in ^{191}Ir and ^{193}Ir

Nuclide	Quantity ^a	ARM ^b	$U(6/4)$ ^c	$U(6/20)$ ^d	Experiment ^e
^{191}Ir	$Q(3/2_1^+)$	+0.546	−0.899	−0.966	+0.816(9)
	$g(3/2_1^+)$	0.094	0.380	0.504	0.1005(4)
	$g(1/2_1^+)$	1.359	0.182	0.540	1.200(12)
	$g(5/2_1^+)$	0.353	0.328	0.474	0.322(22)
	$g(3/2_2^+)$	0.561	0.314	0.301	0.93(27)
	$g(7/2_1^+)$	0.370	0.334	0.350	0.401(18)
	$g(9/2_1^+)$	0.423	0.311	0.397	0.53(5)
	$g(7/2_3^+)$	0.290	0.310	0.289	0.23(9)
	$g(11/2_1^+)$	0.328	0.322	0.320	0.61(17)
	^{193}Ir	$Q(3/2_1^+)$	+0.466	−0.813	−0.879
$g(3/2_1^+)$		0.107	0.381	0.495	0.1091(4)
$g(1/2_1^+)$		1.431	0.182	0.637	1.038(4)
$g(5/2_1^+)$		0.356	0.328	0.468	0.356(16)
$g(3/2_2^+)$		0.529	0.315	0.278	0.69(25)
$g(7/2_1^+)$		0.375	0.335	0.348	0.441(16)
$g(9/2_1^+)$		0.426	0.312	0.394	0.48(4)
$g(7/2_3^+)$		0.296	0.311	0.257	0.33(4)
$g(11/2_1^+)$		0.328	0.323	0.320	0.49(13)

^a Quadrupole moments in eb . See Tables 13–16 for experimental excitation energies of the states.

^b Asymmetric Rotor Model.

^c $U(6/4)$ supersymmetry model.

^d Broken $U(6/20)$ supersymmetry model; see text.

^e Experimental values from Nuclear Data Sheets [22,23] and the present work.

4.2. $U(6/4)$ and $U(6/20)$ supersymmetries

In SUSY schemes, the Hamiltonian is diagonal in the group chain considered, leading to a simple energy formula in terms of a few parameters. These parameters are fitted to a given experimental spectrum to obtain an optimal description of the energy levels. In contrast, the wave functions are fixed from the outset; that is, they are completely independent of the Hamiltonian parameters. Thus matrix elements of an observable depend only on the operator used and are not affected by the fits to the energy spectrum. Clearly, if the operators describing the electromagnetic transitions can be chosen in a parameter free way, these would provide the most stringent tests for the proposed SUSY scheme. For E2 properties, the rank 2 generator of the superalgebra provides a convenient parameter-free choice for the quadrupole operator. Note that the effective E2 charge is determined from the even–even partner following a basic assumption of the SUSY, namely, that the even–even and odd–even partners are described using the same operators. The situation for the M1 operator is complicated by the fact that the rank 1 generator is proportional to the angular momentum operator, and hence it cannot describe M1 transitions. In previous studies, the M1 operator was parametrized so as to obtain an optimal fit to the data. Here, following Refs. [37,38], we adopt a parameter free choice for the M1 operator, more in the spirit of SUSY. The most general M1 operator in the interacting boson–fermion model with s - d bosons is

$$T^{(M1)} = \sqrt{\frac{3}{4\pi}} \left\{ \alpha_1 [d^\dagger \tilde{d}]^{(1)} - \sum_{jj'} \beta_{jj'} [a_j^\dagger \tilde{a}_j]^{(1)} \right\}. \quad (1)$$

In a SUSY scheme, α_1 is determined from the even–even partner as $\alpha_1 = g_B/\sqrt{10}$, where g_B is the g -factor of the 2_1^+ level. A realistic choice for the fermion parameters is to relate them to the matrix elements of the single particle operators

$$\beta_{jj'} = \frac{1}{\sqrt{3}} \langle j || g_l \mathbf{l} + g_s \mathbf{s} || j' \rangle, \quad (2)$$

with the respective g -factors g_l and g_s for the orbital and spin contributions. For the diagonal parameters, this choice yields

$$\beta_{jj} = \sqrt{j(j+1)(2j+1)/3} g_j, \quad (3)$$

where g_j are the Schmidt values for the single-particle g -factors. Note that the factor in front of g_j is part of the fermion angular momentum operator, i.e. $L_j = \sqrt{j(j+1)(2j+1)/3} [a_j^\dagger \tilde{a}_j]^{(1)}$, which explains the factor of $\sqrt{3}$ in the definition of

Table 13
Comparison of E2 transition rates in ^{191}Ir

E_x [keV]	J_i^π	J_f^π	E_γ [keV]	$B(\text{E}2) [e^2\text{b}^2]$			Experiment ^d
				ARM ^a	$U(6/4)$ ^b	$U(6/20)$ ^c	
82	$1/2_1^+$	$3/2_1^+$	82	0.084	0.379	0.476	0.134(7) [22]
129	$5/2_1^+$	$1/2_1^+$	47	0.118	0.057	0.106	0.067(7) ^e
	$5/2_1^+$	$3/2_1^+$	129	0.572	0.379	0.414	0.64(2) ^e
179	$3/2_2^+$	$5/2_1^+$	50	0.058	0.273	0.319	0.21(9) [22]
	$3/2_2^+$	$1/2_1^+$	97	0.307	0.179	0.191	0.38(9) [22]
	$3/2_2^+$	$3/2_1^+$	179	0.209	0	0.001	0.10(2) [22]
343	$7/2_1^+$	$5/2_1^+$	214	0.103	0.084	0.073	0.186(16) ^e
	$7/2_1^+$	$3/2_1^+$	343	0.273	0.379	0.444	0.28(2) ^e
351	$5/2_2^+$	$3/2_2^+$	172	0.018	0.010	0.024	0.028(6) [22]
	$5/2_2^+$	$5/2_1^+$	222	0.001	0.078	0.101	-
	$5/2_2^+$	$1/2_1^+$	269	0.256	0.306	0.319	0.27(4) [22]
	$5/2_2^+$	$3/2_1^+$	351	0.044	0	0.004	0.012(3) [22] 0.020(5) [16]
503	$9/2_1^+$	$7/2_1^+$	160	0.205	0.109	0.121	-
	$9/2_1^+$	$5/2_1^+$	373	0.522	0.401	0.491	0.46(7) ^e
539	$3/2_3^+$	$5/2_2^+$	188	0.021	0	0.077	0.08(3) [22]
	$3/2_3^+$	$3/2_2^+$	360	0.007	0	0.221	0.00009(7) [22]
	$3/2_3^+$	$5/2_1^+$	409	0.068	0	0.001	0.0041(6) [22]
	$3/2_3^+$	$1/2_1^+$	457	0.064	0	0	0.0026(7) [22]
	$3/2_3^+$	$3/2_1^+$	539	0.056	0	0	0.0147(14) [22]
686	$7/2_3^+$	$5/2_1^+$	557	0.073	0	0	0.14(2) [22]
	$7/2_3^+$	$3/2_1^+$	686	0.003	0	0	0.058(52) [22] 0.063(2) [16]
832	$11/2_1^+$	$7/2_1^+$	489	0.476	0.510	0.591	0.46(3) [22]

^a Asymmetric Rotor Model.

^b $U(6/4)$ supersymmetry model.

^c Broken $U(6/20)$ supersymmetry model; see text.

^d Experimental values mainly from Nuclear Data Sheets and the present work. Generally there is reasonable agreement between the values in the literature; however, where there are significant disparities, the alternative values are shown.

^e Present work.

$\beta_{jj'}$. The off-diagonal parameters are all zero except when $j = l - 1/2$ and $j' = l + 1/2$ (or vice versa), in which case they are given by

$$\beta_{l-1/2, l+1/2} = \sqrt{\frac{2l(l+1)}{3(2l+1)}} (-g_l + g_s). \quad (4)$$

For reasons stated above, we shall not dwell on the description of energy levels, but we refer to earlier studies where they have been well tested in the case of $U(6/4)$ [4–7] and note that the $U(6/20)$ results are very similar to those of $U(6/4)$. Instead, we focus here on testing the E2 and M1 properties using realistic, parameter-free operators.

Table 14
Same as Table 13 but in ^{193}Ir

E_x [keV]	J_i^π	J_f^π	E_γ [keV]	$B(\text{E}2)$ [$e^2\text{b}^2$]				
				ARM ^a	$U(6/4)$ ^b	$U(6/20)$ ^c	Experiment ^d	
73	$1/2_1^+$	$3/2_1^+$	73	0.084	0.306	0.392	0.146(6) [23]	0.274(32) [17]
139	$5/2_1^+$	$3/2_1^+$	139	0.508	0.306	0.337	0.54(2) ^e	
180	$3/2_3^+$	$5/2_1^+$	41	0.042	0.218	0.258	-	
	$3/2_2^+$	$1/2_1^+$	107	0.255	0.142	0.152	0.25(5) [23]	
358	$3/2_2^+$	$3/2_1^+$	180	0.208	0	0.001	0.039(6) [23]	0.092(7) [17]
	$7/2_1^+$	$5/2_1^+$	219	0.082	0.069	0.060	0.13(1) ^e	
362	$7/2_1^+$	$3/2_1^+$	358	0.249	0.306	0.363	0.25(1) ^e	
	$5/2_2^+$	$3/2_2^+$	182	0.014	0.008	0.019	0.045(11) [23]	0.19(4) [17]
461	$5/2_2^+$	$1/2_1^+$	289	0.236	0.244	0.258	0.15(3) [23]	0.47(8) [17]
	$5/2_2^+$	$3/2_1^+$	362	0.037	0	0.003	0.009(3) [23]	0.0093(4) [17]
522	$3/2_3^+$	$5/2_2^+$	99	0.022	0	0.037	-	
	$3/2_3^+$	$3/2_2^+$	281	0.008	0	0.064	0.0007(4) [23]	
	$3/2_3^+$	$5/2_1^+$	322	0.082	0	0.003	0.0082(12) [23]	0.0049(17) [17]
	$3/2_3^+$	$1/2_1^+$	388	0.075	0	0.001	0.0032(11) [23]	
557	$3/2_3^+$	$3/2_1^+$	461	0.056	0	0	0.023(3) [23]	
	$9/2_1^+$	$7/2_1^+$	164	0.182	0.087	0.098	-	
559	$9/2_1^+$	$5/2_1^+$	383	0.466	0.319	0.397	0.39(6) ^e	
	$1/2_2^+$	$3/2_3^+$	97	0.382	0.241	0.267	0.36(16) [23]	0.07(3) [66]
	$1/2_2^+$	$3/2_2^+$	377	0.168	0	0.008	0.0027(33) [23]	
	$1/2_2^+$	$5/2_1^+$	418	0.067	0	0.004	0.009(3)	
621	$1/2_2^+$	$3/2_1^+$	557	0.039	0	0.001	-	
	$5/2_3^+$	$5/2_2^+$	197	0.036	0.277	0.311	-	
	$5/2_3^+$	$7/2_1^+$	202	0.020	0	0	-	
	$5/2_3^+$	$3/2_2^+$	379	0.074	0.119	0.150	-	
	$5/2_3^+$	$5/2_1^+$	420	0.005	0	0.004	0.0007(27) [23]	
	$5/2_3^+$	$1/2_1^+$	486	0.006	0	0	-	
857	$5/2_3^+$	$3/2_1^+$	589	0.001	0	0	0.0003(3) [66]	
	$7/2_3^+$	$7/2_1^+$	557	0.026	0	0	0.032(26) ^e	
	$7/2_3^+$	$5/2_1^+$	557	0.069	0	0	0.11(2) ^e	
857	$7/2_3^+$	$3/2_1^+$	686	0.003	0	0	0.052(6) [23]	
	$11/2_1^+$	$7/2_1^+$	489	0.431	0.406	0.476	0.33(2) [17]	

^a Asymmetric Rotor Model.

^b $U(6/4)$ supersymmetry model.

^c Broken $U(6/20)$ supersymmetry model; see text.

^d Experimental values mainly from Nuclear Data Sheets and the present work. Generally there is reasonable agreement between the values in the literature; however, where there are significant disparities, the alternative values are shown.

^e Present work.

The $U(6/4)$ scheme, being the first SUSY proposed, has been well documented in the literature. We refer to the original references [4–7] and the monograph, Ref. [2], for details of the model and various analytical expressions used in the calculation of the electromagnetic moments and transition rates. The E2 operator is taken as the generator of Spin^{BF}(6), that is,

$$T^{(E2)} = \alpha_2 \left\{ [s^\dagger \tilde{d} + d^\dagger s] + [a_{3/2}^\dagger \tilde{a}_{3/2}]^{(2)} \right\}, \quad (5)$$

where the effective charge is determined from the neighboring Pt isotopes as $\alpha_2 = 0.135$ eb. We note that a positive effective charge leads to the wrong sign for the ground-state quadrupole moment, which can be corrected simply by making α_2 negative. However, as the use of a negative boson effective charge is unprecedented, we resist this temptation here. In the M1 operator (1)–(3), the boson g -factor is $g_B = 0.3$, again determined from the Pt isotopes, and the Schmidt value is used with 0.7 quenching of g_s , $g_{3/2} = 0.418$. The $U(6/4)$ results for this choice of operators are presented in Tables 12–16.

It is difficult to justify the truncation of the single-particle levels for protons to the $d_{3/2}$ orbit only, as assumed in the $U(6/4)$ SUSY, and the poor results obtained for the M1 observables are a direct reflection of this restriction. In the $U(6/20)$ SUSY [19–21], all the positive-parity single-particle levels in the shell, namely $s_{1/2}$, $d_{3/2}$, $d_{5/2}$ and $g_{7/2}$ are included. However, the $U(6/20)$ SUSY assumes degeneracy of all the single-particle levels, whereas in fact the total energy splitting in the shell is over 3 MeV. Not

Table 15
Comparison of M1 transition rates in ^{191}Ir

E_x [keV]	J_i^π	J_f^π	E_γ [keV]	$B(\text{M1})$ [μ_N^2]			Experiment ^d
				ARM ^a	$U(6/4)$ ^b	$U(6/20)$ ^c	
82	$1/2_1^+$	$3/2_1^+$	82	0.002	0.003	0.007	0.00082(4) [22]
129	$5/2_1^+$	$3/2_1^+$	129	0.062	0.001	0.040	0.046(1) ^e
179	$3/2_2^+$	$5/2_1^+$	50	0.025	0.001	0.005	0.011(3) [22]
	$3/2_2^+$	$1/2_1^+$	97	0.076	0.001	0.013	0.125(23) [22]
343	$3/2_2^+$	$3/2_1^+$	179	0.041	0	0.056	0.0039(7) [22]
	$7/2_1^+$	$5/2_1^+$	214	0.032	0.002	0.018	0.051(3) ^e
351	$5/2_2^+$	$3/2_2^+$	172	0.081	0.002	0.005	0.113(16) [22]
	$5/2_2^+$	$5/2_1^+$	222	0.018	0.001	0.001	0.0016(5) [3]
	$5/2_2^+$	$3/2_1^+$	351	0.025	0	0.007	0.0113(14) [3]
503	$9/2_1^+$	$7/2_1^+$	160	0.080	0.001	0.051	-
539	$3/2_3^+$	$5/2_2^+$	188	0.029	0	0.047	0.0050(9) [22]
	$3/2_3^+$	$3/2_2^+$	360	0.008	0	0.015	0.0141(14) [22]
	$3/2_3^+$	$5/2_1^+$	409	0.013	0.003	0.020	0.0130(13) [22]
	$3/2_3^+$	$1/2_1^+$	457	0.003	0.002	0.001	0.0036(3) [22]
	$3/2_3^+$	$3/2_1^+$	539	0.006	0.002	0.006	0.0065(5) [22]
686	$7/2_3^+$	$5/2_1^+$	557	0.020	0	0.007	0.017(3) [22]

^a Asymmetric Rotor Model.

^b $U(6/4)$ supersymmetry model.

^c Broken $U(6/20)$ supersymmetry model; see text.

^d Experimental values mainly from Nuclear Data Sheets and the present work. There is reasonable agreement between these and other values in the literature (except where an incorrect lifetime was adopted for the $5/2_1^+$ state).

^e Present work.

surprisingly, the description of M1 properties in a pure $U(6/20)$ scheme is even worse than that of $U(6/4)$. Clearly, a realistic representation of the single-particle energies is essential in order to get a better description of the M1 data. We do this by including the single-particle energies obtained from a standard BCS calculation in the SUSY Hamiltonian and diagonalizing the perturbed Hamiltonian. The quasiparticle energies used in the Hamiltonian to break the SUSY are $E_{1/2} = 34$, $E_{3/2} = 0$, $E_{5/2} = 782$ and $E_{7/2} = 2451$ keV.

The E2 operator is again taken as the generator of $U(6/20)$ SUSY,

$$T^{(E2)} = \alpha_2 \left\{ [s^\dagger \tilde{d} + d^\dagger s] + \sum_{jj'} \gamma_{jj'} [a_j^\dagger \tilde{a}_{j'}]^{(2)} \right\}, \quad (6)$$

with the same effective charge as in the $U(6/4)$ case. The coefficients $\gamma_{jj'}$ in the fermion part are given by: $\gamma_{1/2,3/2} = -\sqrt{12/25}$, $\gamma_{1/2,5/2} = \sqrt{21/50}$, $\gamma_{3/2,3/2} =$

Table 16
Same as Table 15 but in ^{193}Ir

E_x [keV]	J_i^π	J_f^π	E_γ [keV]	$B(M1) [\mu_N^2]$			Experiment ^d	
				ARM ^a	$U(6/4)$ ^b	$U(6/20)$ ^c		
73	$1/2_1^+$	$3/2_1^+$	73	0.003	0.003	0.007	0.0018(1) [23]	
139	$5/2_1^+$	$3/2_1^+$	139	0.063	0.001	0.037	0.056(1) ^e	
180	$3/2_2^+$	$5/2_1^+$	41	0.026	0.001	0.007	-	
	$3/2_2^+$	$1/2_1^+$	107	0.065	0.001	0.010	0.079(11) [23]	0.066(9) [66]
	$3/2_2^+$	$3/2_1^+$	180	0.046	0	0.053	0.0039(5) [23]	0.009(6) [66]
358	$7/2_1^+$	$5/2_1^+$	219	0.082	0.002	0.016	0.056(3) ^e	
362	$5/2_2^+$	$3/2_2^+$	182	0.082	0.002	0.015	0.047(9) [23]	
	$5/2_2^+$	$3/2_2^+$	362	0.021	0	0.008	0.0077(14) [23]	
461	$3/2_3^+$	$5/2_2^+$	99	0.040	0	0.143	0.0048(9) [23]	0.0007(2) [66]
	$3/2_3^+$	$3/2_2^+$	281	0.006	0	0.012	0.016(2) [23]	0.014(2) [66]
	$3/2_3^+$	$5/2_1^+$	322	0.012	0.003	0.002	0.0109(13) [23]	
	$3/2_3^+$	$1/2_1^+$	388	0.002	0.002	0.014	0.0057(7) [23]	
	$3/2_3^+$	$3/2_1^+$	461	0.006	0.002	0.004	0.0082(11) [23]	
522	$9/2_1^+$	$7/2_1^+$	164	0.077	0.001	0.046	0.025(4) [66]	
557	$1/2_2^+$	$3/2_3^+$	97	0.051	0.002	0.005	0.048(13) [23]	0.009(3) [66]
	$1/2_2^+$	$3/2_2^+$	377	0.003	0.005	0.001	0.00036(30) [23]	
	$1/2_2^+$	$1/2_1^+$	484	0.000	0	0.396	0.0007(2) [23]	
	$1/2_2^+$	$3/2_1^+$	557	0.012	0.001	0.008	0.0036(9) [23]	
559	$5/2_3^+$	$5/2_2^+$	197	0.038	0	0.003	0.018(5) [66]	
	$5/2_3^+$	$7/2_1^+$	202	0.016	0	0.002	0.0011(6) [66]	
	$5/2_3^+$	$3/2_2^+$	379	0.001	0	0.020	0.013(4) [66]	
	$5/2_3^+$	$5/2_1^+$	420	0.046	0	0.008	0.115(20) [23]	
	$5/2_3^+$	$3/2_1^+$	589	0.025	0	0.004	0.140(25) [23]	0.010(2) [66]
621	$7/2_3^+$	$7/2_1^+$	557	0.025	0	0.043	0.023(5) ^e	
	$7/2_3^+$	$5/2_1^+$	557	0.021	0	0.008	0.021(3) ^e	

^a Asymmetric Rotor Model.

^b $U(6/4)$ supersymmetry model.

^c Broken $U(6/20)$ supersymmetry model; see text.

^d Experimental values mainly from Nuclear Data Sheets and the present work. Generally there is reasonable agreement between the values in the literature; however, where there are significant disparities, the alternative values are shown.

^e Present work.

$$\sqrt{49/25}, \gamma_{3/2,5/2} = \sqrt{36/25}, \gamma_{3/2,7/2} = \sqrt{48/25}, \gamma_{5/2,5/2} = -\sqrt{3/175}, \gamma_{5/2,7/2} = \sqrt{144/175}, \gamma_{7/2,7/2} = \sqrt{6/7}.$$

The M1 operator has the form described in Eqs. (1)–(4), with the same boson g -factor and the Schmidt values quenched by 0.7. Note that there is a non-diagonal term in this case, $\beta_{3/2,5/2}$, which has a significant effect on M1 transitions. The E2 and M1 matrix elements are calculated numerically using the wave functions obtained from the diagonalization of the perturbed SUSY Hamiltonian. The results are listed next to those of $U(6/4)$ in Tables 12–16. In the tables and the following discussion we refer to these broken SUSY results as $U(6/20)$ for convenience. (The pure $U(6/20)$ results are not presented here, so there is no danger of confusion.)

5. Discussion

The E2 properties of ^{191}Ir and ^{193}Ir have been compared with the triaxial rotor model and $U(6/4)$ SUSY model by McGowan et al. [16,17]. Our results and comparisons of the E2 properties generally support their conclusion that these isotopes are better described by the triaxial rotor model. However, it should be noted that while the agreement is good, it is not perfect. For example, the quadrupole moments of the ground states are underestimated by about 30% and a number of the transition rates differ from experiment by about a factor of two.

Comparison of the $B(E2)$ values in $U(6/4)$ and $U(6/20)$ (Tables 13 and 14) shows that the two are quite similar. This is consistent with the expectation that $B(E2)$ are dominated by the boson core, and therefore, even significant changes in the single particle part have a relatively small effect on the results. We note that the consistently larger values obtained in $U(6/20)$ are a consequence of the larger fermion charges in the E2 operator in Eq. (6) compared with Eq. (5). As a result, agreement of $U(6/20)$ with the data is in some cases worse than $U(6/4)$. The effect of the perturbation of the single-particle energies can be seen in breaking the degeneracy in some E2 transitions, e.g., from the first 1/2, 5/2 and 7/2 levels to the ground state. The only dramatic effect of the perturbation occurs in $B(E2; 3/2_3 \rightarrow 3/2_2)$, which is sizable here but vanishes in $U(6/4)$ and in the pure $U(6/20)$ case.

The above E2 results confirm that one needs to look at the M1 properties to distinguish between the SUSY schemes, i.e. to probe the single-particle distributions directly, and thus provide a more critical test.

The particle-triaxial-rotor model description of the g -factors is very good, but it should be noted that the rotational g -factor and the quenching factor for the spin part of the single-nucleon g -factor were chosen to give this agreement. Once adequate agreement with the static moments was obtained we did not further tune the parameters either to improve the static moments or the transition rates. The M1 transition rates are generally predicted within about a factor of two, with a satisfactory tracing of the experimental trends; i.e. strong M1 transitions are usually predicted to be strong and weak M1 transitions are generally predicted to be weak. The similar calculations by Vieu et al. [3], who did not quench the spin g -factor from its free-nucleon value, show about the same level of agreement between theory and experiment. Although the description of the M1 properties in the SUSY models is much worse, it should be kept in mind that there is no scope at all for tuning the M1 parameters in those models.

Comparison of g -factors in Table 12 shows that while there are some improvements (notably $1/2_1$) in going from $U(6/4)$ to $U(6/20)$, this is not uniform and for some states the agreement actually gets worse. One can presumably improve the description of g -factors by adjusting the quasiparticle energies obtained from the BCS calculations, though we do not attempt it here. The $B(M1)$ values presented in Tables 15 and 16 paint a completely different picture: they are more than an order of magnitude smaller than the measured values in $U(6/4)$ whereas $U(6/20)$ provides a more reasonable description of the data. Thus the use of a realistic M1 operator (including the consistent choice of parameters) exposes the inadequacy of the truncation of the single particle levels to the $d_{3/2}$ orbit. Again there are a few transitions which have small measured $B(M1)$ values and vanish in $U(6/4)$ (e.g., $3/2_3 \rightarrow 5/2_2$ and $1/2_2 \rightarrow 1/2_1$), but are amplified to quite large values in $U(6/20)$ as a result of perturbation-induced mixing. Notwithstanding these few anomalous cases, overall, $U(6/20)$ provides a much better description of the M1 transitions than $U(6/4)$.

Extension of the $U(6/4)$ to $U(6/20)$ SUSY was first suggested by Zhu [20] in order to improve on the large symmetry breaking observed in the $^{194,196,198}\text{Pt}(t, \alpha)^{193,195,197}\text{Ir}$ single-particle transfer experiments [9,10]. Due to the increased number of fitted parameters in the transfer operator (from one to four), it is difficult to assess whether the improved description of the transfer strengths obtained in $U(6/20)$ is a genuine feature of the model or not. In this respect, the recent transfer experiments that connect ^{195}Pt with both its even–even and odd–odd partners in the $U_\nu(6/12) \otimes U_\pi(6/4)$ supermultiplet offer a much more thorough test of the proposed SUSY scheme [69]. It would be interesting to perform similar studies on the iridium isotopes to see if a complementary description of the transfer data can be obtained in $U(6/20)$.

6. Summary and conclusions

The electromagnetic properties of the low-lying natural-parity states in ^{191}Ir and ^{193}Ir were studied following Coulomb excitation, thereby extending the data set and resolving discrepancies in earlier work. The present and previously compiled E2 and M1 data were used in parameter-free tests of the $U(6/4)$ and broken $U(6/20)$ SUSY models, with triaxial rotor model calculations, which provide a good description of both the E2 and M1 observables, serving as a benchmark for comparison.

Qualitatively, a similar level of agreement between the $U(6/4)$ and $U(6/20)$ models is found for E2 transitions, although the $U(6/20)$ results are slightly inflated compared with those from $U(6/4)$ due to larger effective charges in the fermion sector of the E2 operator.

Comparison of the M1 data with the predictions of the two SUSY schemes, however, gives a very different perspective: it clearly demonstrates the inadequacy of the single- j $U(6/4)$ SUSY in describing the M1 transitions, and shows the necessity of including other orbits in a multi- j SUSY such as $U(6/20)$.

In comparison with the $U(6/12)$ SUSY model which described the g -factors of excited states in ^{195}Pt very well [37,38], the $U(6/20)$ model as applied to ^{191}Ir and ^{193}Ir is found to be less successful. One reason for this is that the splitting of the single-particle energies is quite large in $U(6/20)$, which necessitates their inclusion in the Hamiltonian via a perturbation. While the BCS procedure used for this purpose gives a

reasonable ordering of single-particle levels, it cannot be expected to provide the accuracy (\sim tens of keV) required to mix the $s_{1/2}$ and $d_{3/2}$ levels correctly.

Acknowledgements

We would like to thank our colleagues Dr S.S. Anderssen, Dr S. Bayer, Dr A.P. Byrne, Dr P.M. Davidson, Dr T. Kibédi, Dr F.G. Kondev, Dr G.J. Lane, Dr S.M. Mullins, T.R. McGoram and Dr N.M. Thakur for their assistance with the data collection. We are grateful to Professor N. Benczer-Koller and J. Holden (Rutgers University) for assistance with the magnetization measurements. W.A.S. thanks the Australian National University for a Visiting Fellowship and FAPESP (São Paulo) for financial support. This work was supported, in part, by the Australian Research Council.

References

- [1] A. Bohr, B.R. Mottelson, *Nuclear Structure*, Vol. II (W.A. Benjamin, Reading, MA, 1975).
- [2] F. Iachello, P. Van Isacker, *Interacting Boson–Fermion Model* (Cambridge University Press, Cambridge, 1988).
- [3] Ch. Vieu, S.E. Larsson, G. Leander, I. Ragnarsson, W. De Wiclawik, J.S. Dionisio, *Z. Phys. A* 290 (1979) 301.
- [4] F. Iachello, *Phys. Rev. Lett.* 44 (1980) 772.
- [5] A.B. Balantekin, I. Bars, F. Iachello, *Phys. Rev. Lett.* 47 (1981) 19.
- [6] A.B. Balantekin, I. Bars, F. Iachello, *Nucl. Phys. A* 370 (1981) 284.
- [7] F. Iachello, S. Kuyucak, *Ann. Phys.* 136 (1981) 19.
- [8] M.N. Harakeh, P. Goldhorn, Y. Iwasaki, J. Lukasiak, L.W. Put, S.Y. van der Werf, F. Zwarts, *Phys. Lett. B* 97 (1980) 21.
- [9] J.A. Cizewski, D.G. Burke, E.R. Flynn, R.E. Brown, J.W. Sunier, *Phys. Rev. Lett.* 46 (1981) 1264.
- [10] J.A. Cizewski, D.G. Burke, E.R. Flynn, R.E. Brown, J.W. Sunier, *Phys. Rev. C* 27 (1983) 1040.
- [11] Y. Iwasaki, E.H.L. Aarts, M.N. Harakeh, R.H. Siemssen, S.Y. van der Werf, *Phys. Rev. C* 23 (1981) 1477.
- [12] W.M. Lattimer, K.S. Krane, N.J. Stone, G. Eska, *J. Phys. G* 7 (1981) 1713.
- [13] H.H. Ghaleb, K.S. Krane, *Nucl. Phys. A* 426 (1984) 20.
- [14] S.J. Mundy, J. Lukasiak, W.R. Phillips, *Nucl. Phys. A* 426 (1984) 144.
- [15] W.R. Kölbl, J. Billowes, J. Burde, J.A.G. De Raedt, M.A. Grace, A. Pakou, *Nucl. Phys. A* 456 (1986) 349.
- [16] F.K. McGowan, N.R. Johnson, I.Y. Lee, W.T. Milner, C. Roulet, J. Hattula, M.P. Fewell, Y.A. Ellis-Akovi, R.M. Diamond, F.S. Stephens, M.W. Guidry, *Phys. Rev. C* 33 (1986) 855.
- [17] F.K. McGowan, N.R. Johnson, I.Y. Lee, W.T. Milner, C. Roulet, R.M. Diamond, F.S. Stephens, M.W. Guidry, *Phys. Rev. C* 35 (1987) 968.
- [18] A.B. Balantekin, I. Bars, R. Bijker, F. Iachello, *Phys. Rev. C* 27 (1983) 1761.
- [19] Y.S. Ling, M. Zhang, J.M. Xu, M. Vallieres, R. Gilmore, D.H. Feng, H.Z. Sun, *Phys. Lett. B* 148 (1984) 13.
- [20] P.Y. Zhu, *Nuovo Cimento A* 90 (1986) 308.
- [21] J. Jolie, K. Heyde, P. Van Isacker, A. Frank, *Nucl. Phys. A* 466 (1987) 1.
- [22] E. Browne, S.Y. Chu, *Nuclear Data Sheets* 74 (1995) 611.
- [23] V.S. Shirley, *Nuclear Data Sheets* 61 (1990) 519.
- [24] F.K. McGowan, P.H. Stelson, *Phys. Rev.* 109 (1958) 901.
- [25] J. Lindskog, T. Sundström, P. Sparman, *Z. Phys.* 710 (1962) 347.
- [26] E.E. Berlovich, Y.K. Gusev, V.V. Ilin, M.K. Nikitin, *Soviet Phys. JETP* 16 (1963) 1144.
- [27] R. Avida, J. Burde, A. Molchadzki, *Nucl. Phys. A* 115 (1968) 405.
- [28] R. Avida, M.B. Goldberg, G. Goldring, A. Sprinzak, *Nucl. Phys. A* 135 (1969) 678.
- [29] T. Badica, A. Gelberg, C. Protop, S. Salageanu, *Rev. Roum. Phys.* 14 (1969) 471.

- [30] J. Lindskog, K.G. Valivaara, Z. Awwad, S.E. Hagglund, A. Marelius, J. Phil, Nucl. Phys. A 137 (1969) 511.
- [31] S.G. Malmkog, A. Bäcklin, Ark. Fys. 39 (1969) 411.
- [32] W.R. Owens, B.L. Robinson, S. Jha, Phys. Rev. 185 (1969) 1555.
- [33] P. Steiner, E. Gerda, W. Hautsch, D. Steenken, Z. Phys. 221 (1969) 281.
- [34] V. Berg, S.G. Malmkog, A. Bäcklin, Nucl. Phys. A 143 (1970) 177.
- [35] P. Norgaard, K.M. Bisgard, K. Gregersen, P. Morgen, Nucl. Phys. A 162 (1971) 449.
- [36] R.A. Wagoner, J.G. Mullen, G. Schupp, Phys. Rev. C 47 (1993) 1951.
- [37] S. Kuyucak, A.E. Stuchbery, Phys. Rev. C 48 (1993) R13.
- [38] G.J. Lampard, A.E. Stuchbery, H.H. Bolotin, S. Kuyucak, Nucl. Phys. A 568 (1994) 617.
- [39] A.E. Stuchbery, E. Bezakova, Phys. Rev. Lett. 82 (1999) 3637.
- [40] A.E. Stuchbery, S.S. Anderssen, E. Bezakova, Hyp. Int. 97/98 (1996) 479.
- [41] A.E. Stuchbery, C.G. Ryan, H.H. Bolotin, I. Morrison, S.H. Sie, Nucl. Phys. A 365 (1981) 317.
- [42] A.E. Stuchbery, Ph.D. thesis (University of Melbourne, 1982), unpublished.
- [43] A.E. Stuchbery, I. Morrison, L.D. Wood, R.A. Bark, H. Yamada, H.H. Bolotin, Nucl. Phys. A 435 (1985) 635.
- [44] A.P. Byrne, A.E. Stuchbery, H.H. Bolotin, C.E. Doran, G.J. Lampard, Nucl. Phys. A 466 (1987) 419.
- [45] A.E. Stuchbery, G.J. Lampard, H.H. Bolotin, Nucl. Phys. A 642 (1998) 361.
- [46] M.P. Robinson, A.E. Stuchbery, E. Bezakova, S.M. Mullins, H.H. Bolotin, Nucl. Phys. A 647 (1999) 175.
- [47] S.S. Anderssen, A.E. Stuchbery, S. Kuyucak, Nucl. Phys. A 593 (1995) 212.
- [48] A.E. Stuchbery, E. Bezakova, Austr. J. Phys. 51 (1998) 183.
- [49] A. Piqué, J.M. Brennan, R. Darling, R. Tanczyn, D. Ballon, N. Benczer-Koller, Nucl. Inst. Meth. A 279 (1989) 579.
- [50] J.F. Ziegler, J.P. Biersack, U. Littmark, The stopping and range of ions in solids, in: The stopping and ranges of ions in matter, Vol. 1, J.F. Ziegler, ed. (Permagon, New York, 1985).
- [51] R.J. Sturm, M.W. Guidry, Nucl. Instr. Meth. 138 (1976) 507.
- [52] A.E. Stuchbery, Nucl. Instr. Meth. Phys. Res. A 385 (1997) 547.
- [53] H.H. Bolotin, A.E. Stuchbery, I. Morrison, D.L. Kennedy, C.G. Ryan, S.H. Sie, Nucl. Phys. A 370 (1981) 146.
- [54] O. Häusser, H.R. Andrews, D. Ward, N. Rud, P. Taras, R. Nicole, J. Keinonen, P. Skensved, C.V. Stager, Nucl. Phys. A 406 (1983) 339.
- [55] O. Häusser, H.R. Andrews, D. Horn, M.A. Lone, P. Taras, P. Skensved, R.M. Diamond, M.A. Deleplanque, E.L. Dines, A.O. Macchiavelli, F.S. Stephens, Nucl. Phys. A 412 (1984) 141.
- [56] N.K.B. Shu, D. Melnik, J.M. Brennan, W. Semmler, N. Benczer-Koller, Phys. Rev. C 21 (1980) 1828.
- [57] R. Tanczyn, G. Kumbartzki, A. Piqué, T. Vass, A. Pakou, N. Benczer-Koller, Phys. Rev. C 48 (1993) 140.
- [58] A.E. Stuchbery, T.H. Heseltine, S.S. Anderssen, H.H. Bolotin, A.P. Byrne, B. Fabricius, T. Kibédi, Hyperfine Interactions 88 (1994) 97.
- [59] S. Raman, C.H. Malarkey, W.T. Milner, C.W. Nestor Jr., P.H. Stelson, Atom. Data & Nucl. Data Tables 36 (1987) 1.
- [60] S.S. Anderssen, A.E. Stuchbery, Hyperfine Interactions 96 (1995) 1.
- [61] S. Gustafsson, K. Johansson, E. Karlsson, L.-O. Norlin, Å.G. Svensson, Arkiv Fys. 34 (1967) 169.
- [62] R. Avida, I. Ben Zvi, P. Gilad, M.B. Goldberg, G. Goldring, K.H. Speidel, A. Sprinzak, Nucl. Phys. A 147 (1970) 200.
- [63] N.A. Ilkhamdzhonov, P.S. Radzhapov, K.T. Salikhbaev, Izv. Akad. Nauk Uzb. SSR Ser. Fiz.-Mat. Nauk 4 (1973) 79.
- [64] A.V. Davydov, M. M Korotkov, P.I. Romasheva, Izv. Akad. Nauk SSSR Ser. Fiz. 44 (1980) 1778.
- [65] F.E. Wagner, Hyp. Int. 13 (1983) 149.
- [66] S.-E. Drissi, Nucl. Phys. A 621 (1997) 655.
- [67] P.B. Semmes, I. Ragnarsson, The particle + triaxial rotor model. A user's guide, unpublished, distributed at the Hands-on nuclear theory workshop, Oak Ridge (5–16 August, 1991), and references therein.
- [68] T. Bengtsson, I. Ragnarsson, Nucl. Phys. A 436 (1985) 14.
- [69] A. Metz, J. Jolie, G. Graw, R. Hertenberg, J. Gröger, C. Günther, N. Warr, Y. Eisermann, Phys. Rev. Lett. 83 (1999) 1542.